(ct)Interferometric Synthetic Aperture Microscopy

Steven G. Adie, Brynmor J. Davis, Tyler S. Ralston, Daniel L. Marks, P. Scott Carney and Stephen A. Boppart

(1)Introduction

The history of imaging is replete with examples describing the development of data acquisition systems followed later by the mathematical and computational infrastructure necessary to turn the acquired data into quantitatively meaningful and more practically useful images. For example, while Roentgen discovered a means to record x-ray intensities on film at the turn of the 20th century, more than half a century elapsed until the computational power was available to turn a series of x-ray shadowgrams into a computed tomogram. In 1991, the evolution of optical coherence tomography (OCT) [1] from low-coherence interferometry (LCI) [2] was followed by many years of technology development and application, most prolifically in the medical and biological fields. Despite this rapid development, little was done to connect the acquired data to the underlying sample structure as described by the spatially varying scattering potential, until the development of interferometric synthetic aperture microscopy (ISAM) in 2006 [3]. The delay between the development of OCT instrumentation and a solution and implementation of the associated inverse problem might be attributed, at least in part, to the success of OCT as a direct imaging method. The use of OCT as an instrument for data acquisition is apparent in the so-called trade off between transverse resolution and depth of imaging. The apparent degradation of OCT images associated with regions far from focus was not a pressing concern, largely because low numerical aperture optics were used to focus light into tissue, thereby offering a large confocal parameter (depth-of-field) for cross-sectional imaging, at the expense of reduced (worse) transverse imaging resolution. Higher (better) transverse resolutions were achieved by using higher numerical aperture (NA) focusing optics, and performing optical coherence microscopy (OCM) [4]. OCM captures images in the *en face* plane in a manner similar to confocal or multiphoton microscopy, rather than in cross-section using OCT. The development of spectral-domain OCT (SD-OCT) [5-8] provided a number of distinct advantages for ISAM. However, using early time-domain OCT (TD-OCT) systems or SD-OCT

systems, it was practical only to acquire data from the in-focus region. Absent a solution of the inverse problem, it was common (especially when higher NA optics are employed) to discard the acquired data associated with regions out of the focus. With ISAM, not only is the data quantitatively and meaningfully connected to the sample structure, but the entire sample is also reconstructed at arbitrary distances from the focus and the supposed trade-off between depth of imaging and resolution is eliminated. With ISAM, depth of imaging is limited only by the signal-to-noise ratio (SNR) and the advent of multiple scattering.

A brief overview of OCT instrumentation and applications is presented in the following section. The physics of the data acquisition system, *i.e.*, the mathematical forward model relating the data to the sample, is described in Section 3. This forward model is inverted to find an inverse scattering algorithm, *i.e.*, a means to obtain quantitative estimate of the sample scattering potential from the data. It is seen that the mathematical structure of the inverse problem is similar to that encountered in a broad class of applications where the solution of the inverse problem can be reduced to Fourier domain resampling. This class of applications includes computed tomography, diffraction tomography, and magnetic resonance imaging. In fact, for a particular ISAM modality the Fourier resampling scheme is identical to that used in synthetic aperture radar (SAR). In Section 4, experimental implementation and validation of ISAM are described. Material dispersion and phase instability corrections are described before a controlled synthetic sample is used to characterize ISAM. Furthermore, ISAM images computed from out-of-focus data are compared to in-focus OCT images taken in the same volume and are shown to be in good agreement. Fast implementation of the ISAM software is described before the limitations of ISAM are discussed. In Section 5, clinical and biological applications that take advantage of the unique capabilities of ISAM are discussed. Section 6 summarizes the main theoretical, experimental, and application aspects of ISAM, and concludes with an outlook on future directions.

(2)Background

Optical coherence tomography instrumentation is illustrated in Figure 1. A sample is probed using a broadband optical source. The illuminating light is focused into the

sample and the backscattered light is collected through the same objective lens. The two transverse (x, y) dimensions are probed by either physically translating the sample or scanning the focal spot. The scattering potential is resolved in the axial z dimension through LCI. That is, the backscattered light is combined with a reference field in order to produce interference. In time-domain OCT, interference effects are only observed when the roundtrip path lengths in the sample and reference arms are within the coherence length of the source. Interference fringes that constitute the desired interference signal can be easily isolated from the constant background, with the result that only the scattering potential at a given axial depth affects the acquired signal. The probed depth is where the sample-arm path length is equal to that given in the reference arm. Thus a depth profile is obtained by scanning the reference arm path length. Equivalent data are collected using a spectral-domain OCT system [9]. In this case the reference mirror is fixed and a spectrometer replaces the single broadband detector employed in time-domain systems. Raw data acquired in SD-OCT are the Fourier transform of the time-domain data (with respect to delay). For this reason, SD-OCT is also referred to as Fourier-domain OCT (FD-OCT). The use of SD-OCT enables both high-speed data acquisition and high sensitivity [7, 10, 11] and the use of a static reference arm, with superior phase stability, presents an additional advantage for ISAM data acquisition.
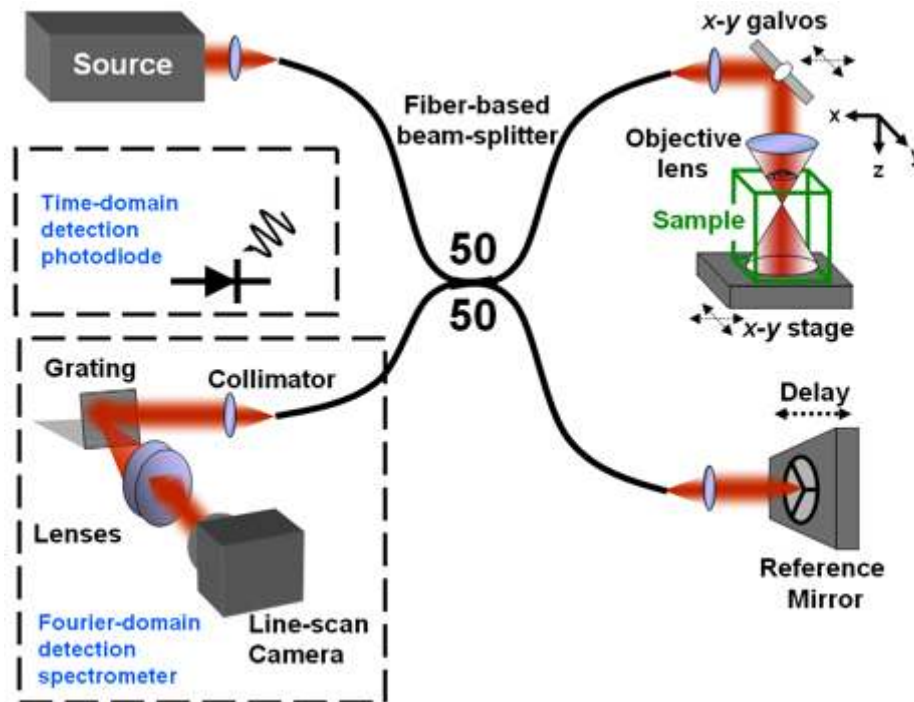
Figure 1: Schematic of time-domain and spectral-domain OCT systems. Light in one arm of a fiber-based Michelson interferometer is focused into the sample, while the other arm is used as a reference. In TD-OCT, the length of the reference path is adjusted and an interferogram is measured with a photodiode. In SD-OCT, the reference arm is fixed and the spectral interference measured with a spectrometer. This figure is adapted from [3].

For biological applications, OCT is typically implemented using near-infrared wavelengths, because in this region, the optical response of tissue is typically dominated by scattering rather than absorption [12]. OCT therefore allows good depth of penetration, while the coherence gating used for detection has the effect of rejecting some of the multiply scattered light that renders standard optical microscopes impractical. OCT offers micron-scale resolution enabling image contrast based on intrinsic sample properties, *i.e.*, the scattering potential. This has led to extensive use of OCT in retinal imaging [13]. OCT has also been applied with good success to the detection of vulnerable arterial plaques *in vivo* [14], and for long-scan-range *in vivo* monitoring of upper airway profiles in the study of sleep apnea [15]. Other application areas are cancer

detection in various parts of the body including the breast [16], gastrointestinal tract [17], bladder [18], skin [19], oral cavity [20], cervix [21], lung [22], and brain [23].

Transverse localization is achieved in OCT data through the focusing of the illuminating light and the focused detection of the backscattered light. The power of this focusing is in turn determined by the objective lens used. The larger the numerical aperture (NA) of the lens, the tighter the resulting focus. This effect can be seen in Figure 2, where focused beams are illustrated for a number of NAs. The relationship between the transverse resolution and the depth of field is also illustrated in Figure 2. A tightly focused beam diverges faster than a beam with a wider focus. Quantitatively, the focal width scales with $1/NA$, while the depth of focus scales as $1/NA^2$. Thus the raw data in OCT appear to suffer from a trade-off between transverse resolution and depth-of-field.
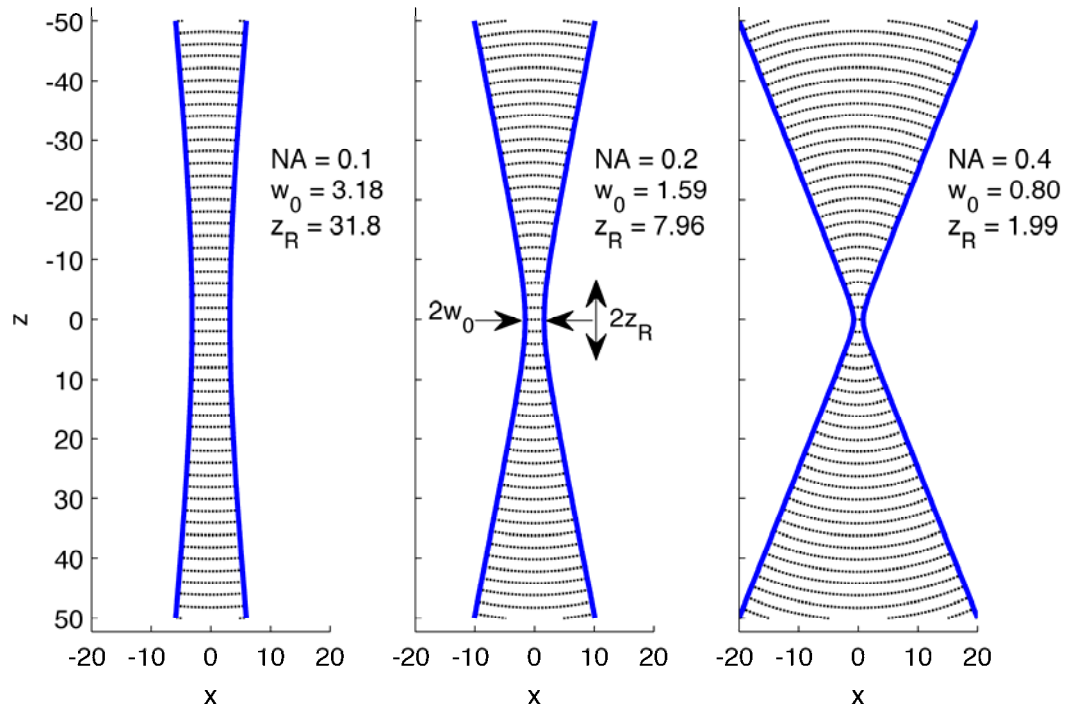

Figure 2: Scale drawings of focused fields, based on a Gaussian beam model [24], where all spatial dimensions are in units of wavelength. The beam edge is defined as the loci at which the field reaches $1/e$ of the maximum value and is illustrated with a heavy line. Every second oscillation of the phase is illustrated by a dotted line showing a wavefront. The NA is the sine of the angle the beam edge makes with the

optical axis far from the focus, w_0 is a measure of the narrowest point of the beam and $2z_R$ is the confocal parameter quantifying the depth-of-field.

Axial discrimination in OCT images is provided by coherence gating, with the axial resolution determined, with an inverse relationship, by the bandwidth of the optical source. Volumes of the sample that fall within the beam focus are well imaged, but those that lie out of the focus are subject to transverse blurring and the generation of coherent artifacts sometimes referred to as speckle. The fundamental relationship between depth-of-focus and minimum beam-width illustrated in Figure 2 has lead to the idea that depth-of-field and transverse resolution are competing constraints in OCT. As will be seen, computational image reconstruction can be used to obviate this apparent trade-off.

(3)Theory

(3.1) Physics of data acquisition

The sample to be imaged is described by a function η on three Cartesian axes (x, y, z). The spectral-domain data are collected as a function of two transverse scan positions (u, v) and the temporal frequency ω of the optical field. The relationship between the spatial variables is illustrated in Figure 3.
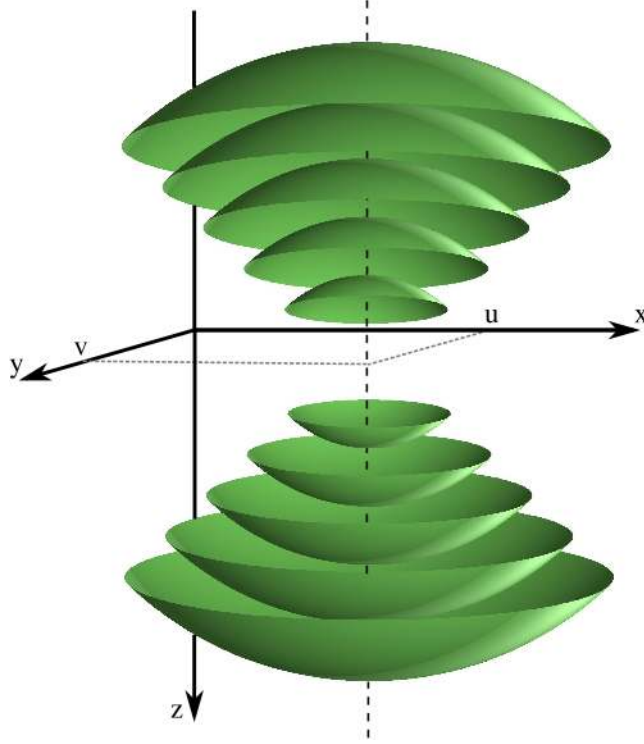
Figure 3: Illustration of the system geometry and the behavior of the incident optical field. The geometrical focus lies in the *x-y* plane within the object and the focal position is scanned through these two transverse dimensions. A heavy dashed line indicates the optical axis of the objective lens, which has a position specified by the variables *u* and *v*. Away from focus the field diverges and, for a fixed frequency ω, has approximately spherical phase fronts.

It will be convenient to exchange the temporal frequency ω for an equivalent variable more directly related to the spatial structure of the optical field. The wavenumber $k = 2\pi/\lambda$, where λ is the wavelength, in free space can be expressed as

$$k = \frac{\omega}{c} \tag{1.1}$$

where c is the speed of light. More complex, nonlinear dispersion relationships between ω and k can account for propagation in materials where the index of refraction varies with the temporal frequency of the field [25, 26].

After extracting the analytic interferometric term from the collected data [9], the signal is described by the product

$$S(u,v,k) = E_r^*(k) E_s(u,v,k) \tag{1.2}$$

where $E_s(u,v,k)$ is the backscattered field at the detector, $E_r(k)$ is the reference field and a superscript $*$ denotes the complex conjugate.

The optical properties of the sample are described by the scattering potential $\eta(x,y,z)$, which can also be identified, in terms of fundamental material properties, as the susceptibility. An accurate reconstruction of $\eta(x,y,z)$ is the goal in ISAM. The sample is illuminated by an electric field proportional to $E_r(k) g(x-u, y-v, z, k)$, where the reference field $E_r(k)$ is proportional to the source field and hence also to the amplitude of illumination. Scattering produces optical sources with density $k^2 E_r(k) g(x-u, y-v, z, k) \eta(x,y,z)$, where it can be seen that the amplitude of the scattered light is proportional to both the illuminating field and the scattering potential.

Reciprocity [27] requires that coupling the light back into the optical system that produced the illuminating field will introduce into the signal another factor of the beam pattern, $g(x-u, y-v, z, k)$. Integrating over all scattering locations results in the expression

$$E_s(u,v,k) = k^2 E_r(k) \iiint g^2(x-u, y-v, z, k) \eta(x,y,z) \, dx \, dy \, dz \tag{1.3}$$

for the backscattered field. Here it can be seen that the scattered field is linearly related to the sample scattering potential through an integral equation. The kernel of this equation depends on the square of the focused field produced by the objective lens. Scattering from sample areas at the focus contribute more signal than scattering from areas out of focus. For the purposes of OCT, $g^2(x-u, y-v, z, k)$ is ideally a narrow, well-collimated beam, giving high transverse resolution and good depth of field. Depth (axial) resolution is achieved using the spectral diversity of the data. However, as demonstrated in Figure 2, a Gaussian optical beam cannot be simultaneously narrow and well collimated.

The results obtained with ISAM are achieved by inverting Eq. (1.3), to obtain an accurate estimate for $\eta(x,y,z)$ both at and away from focus, *i.e.*, ISAM is accomplished by implementing inverse scattering. In Section 3.2 we derive a simplified forward model

for ISAM based upon a spherical beam model for the focused field, while Section 3.3 employs a general description of the focused field to obtain a rigorous forward model. Section 3.4 follows with a method to invert the forward model and obtain an estimate for $\eta(x, y, z)$.

(3.2) Compact forward model

Before presenting a detailed picture of the theory of ISAM, it is instructive to give a simplified explanation that captures the essential physics of the system while simplifying the mathematics. The derivation presented in this Section is valid when the wavefronts in the incident field are spherical and at small angles from the optical axis, *i.e.* well beyond the depth-of-focus, and for low NA. The principal problem addressed by ISAM is manifest outside the depth-of-focus, in the divergent-beam regions as illustrated in Figure 2 and Figure 3. In these areas the beam broadens and the phase fronts (which are well-defined for a given value of k) become spherical. Consider as simplified model of the focused field a spherical wave propagating in the downward $(+z)$ direction, *i.e.*,

$$g(x, y, z, k) = \frac{\exp\left[i\sigma k \sqrt{x^2 + y^2 + z^2}\right]}{\sqrt{x^2 + y^2 + z^2}}, \qquad (1.4)$$

where $\sigma = \mathrm{sgn}(z)$. This model does not account for the beam profile (e.g. the numerical aperture of the objective lens does not appear in this model) but, as will be verified in Section 3.3, it captures the basic phase behavior and features of the ISAM algorithm.

Combining Eqs. (1.2), (1.3) and (1.4) results in the model

$$S(u, v, k) = k^2 |E_r(\omega)|^2 \iiint \frac{\exp\left[i\sigma 2k \sqrt{(x-u)^2 + (y-v)^2 + z^2}\right]}{(x-u)^2 + (y-v)^2 + z^2} \eta(x, y, z)\, dx\, dy\, dz. \qquad (1.5)$$

Here the phase of the data is referenced to the focal point. The signal from each scattering location acquires a phase delay corresponding to the round-trip path from the focus to the scattering site and back. The signal is linearly attenuated by spreading losses in each propagation direction and all contributions are summed to produce the data.

Simply restating Eq. (1.5) in a more convenient form yields the forward model used in ISAM. The simplification is achieved by the use of the Weyl identity [28, 29], where a spherical wave is constructed as a sum of plane waves, *i.e.*,

$$\frac{\exp\left[i\sigma\kappa\sqrt{x^2+y^2+z^2}\right]}{\sqrt{x^2+y^2+z^2}} = \frac{i}{2\pi}\iint\frac{\exp\left[i\left(q_x x+q_y y+\sqrt{\kappa^2-q_x^2-q_y^2}\,z\right)\right]}{\sqrt{\kappa^2-q_x^2-q_y^2}}\,dq_x dq_y, \qquad (1.6)$$

where $(q_x,q_y,\sqrt{\kappa^2-q_x^2-q_y^2})$ is the wavevector of the constituent plane waves. Comparing this to Eq. (1.5), it can be seen that the choice $\kappa=2k$ is appropriate, so that

$$S(u,v,k) = \frac{ik^2}{2\pi}\left|E_r(\omega)\right|^2\iint\frac{1}{\sqrt{4k^2-q_x^2-q_y^2}}\exp\left[i\left(q_x u+q_y v\right)\right]$$

$$\left[\iiint\frac{\eta(x,y,z)}{\sqrt{(x-u)^2+(y-v)^2+z^2}}\exp\left[-i\left(q_x x+q_y y-\sqrt{4k^2-q_x^2-q_y^2}\,z\right)\right]dx\,dy\,dz\right]dq_x dq_y$$

.
$$(1.7)$$

The quotient in the inner integral will be approximated as

$$\frac{\eta(x,y,z)}{\sqrt{(x-u)^2+(y-v)^2+z^2}} \approx \frac{\eta(x,y,z)}{z}. \qquad (1.8)$$

This approximation can be justified for low NA, as outside of $z^2 \gg (x-u)^2+(y-v)^2$ the limited extent of the focused beam will typically give low signal, and in high-signal areas the unapproximated denominator will be slowly varying. For high-NA systems this approximation will be less accurate, and the detailed derivation of ISAM presented in Section 3.3 must be used.

Returning to Eq. (1.7), a three-dimensional Fourier transform and a two-dimensional inverse Fourier transform can be recognized. The transverse Fourier transform of the data will be denoted by $\tilde{S}(q_x,q_y,k)$, and the three-dimensional Fourier transform of $\eta(x,y,z)/z$ will be denoted by $\tilde{\tilde{\eta}}'(q_x,q_y,\beta)$. Rewriting Eq. (1.7) using these definitions gives

$$\tilde{S}\left(q_x, q_y, k\right) = \frac{i\pi k^2}{k_z\left(\dfrac{q_x}{2}, \dfrac{q_y}{2}\right)} \left|E_r\left(\omega\right)\right|^2 \tilde{\tilde{\eta}}'\left[q_x, q_y, -2k_z\left(\frac{q_x}{2}, \frac{q_y}{2}\right)\right], \tag{1.9}$$

where k_z is the function

$$k_z\left(q_x, q_y\right) = \sqrt{k^2 - q_x^2 - q_y^2} \ . \tag{1.10}$$

It should be noted that, strictly speaking, $k_z\left(q_x, q_y\right)$ is a function of k, but for simplicity this dependence is taken to be implied.

The multiplex spatial-domain relationship of Eq. (1.5) is reduced to a one-to-one Fourier-domain relationship in Eq. (1.9). Each point in the two-dimensional Fourier transform of the k-domain data is proportional to a point in the three-dimensional Fourier transform of the sample (with a factor z^{-1} included). Inherent in the forward model presented here is the axial mapping between the Fourier space of the data and the Fourier space of the object, given by

$$\begin{aligned} \beta &= -2k_z\left(\frac{q_x}{2}, \frac{q_y}{2}\right) \\ &= -\sqrt{4k^2 - q_x^2 - q_y^2} \end{aligned} \tag{1.11}$$

This mapping, illustrated in Figure 4, suggests a simple inverse scattering method based on the remapping of data Fourier space to the object Fourier space. Further details are presented in Section 3.4.
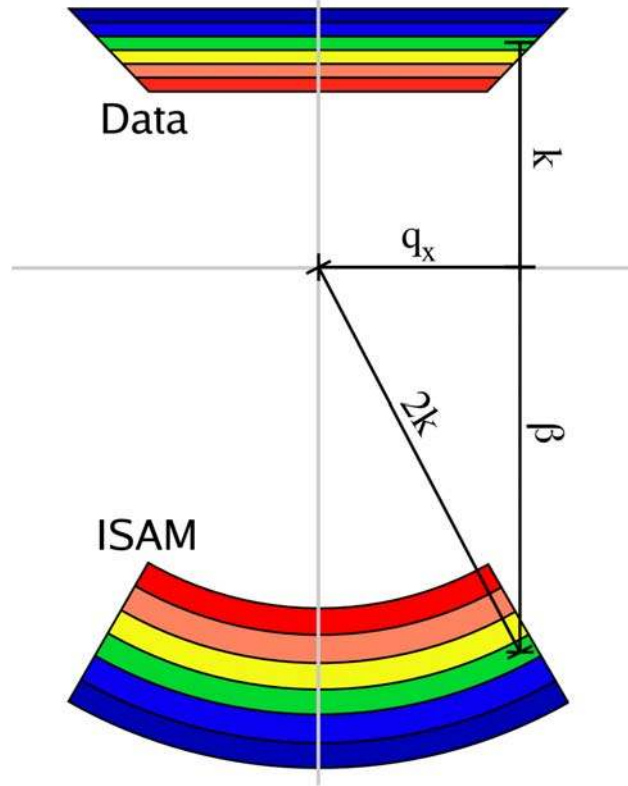
Figure 4: Illustration of the ISAM remapping for a cross-sectional plane – the three-dimensional contours are cylindrically symmetric about the vertical axis. In general, Fourier-domain data are a function of transverse spatial frequencies (q_x, q_y) and wavenumber k. These coordinates are mapped to the three spatial frequency coordinates (q_x, q_y, β) in the Fourier domain representation of the sample. This mapping is such that $q_x^2 + q_y^2 + \beta^2 = 4k^2$.

Image reconstruction in basic OCT usually consists of scaling the axial dimension according to the elementary model that a scatterer at depth z acquires an offset of twice its depth, so that

$$\beta = -2k .$$ (1.12)

This approach may be justified near focus as a coarse approximation of the ISAM result in Eq. (1.11). However, as will be seen below, the ISAM method corrects out-of-focus blur, while the standard OCT method does not.

The coordinate relation given in Eq. (1.11) is known as the Stolt mapping [30, 31]. This coordinate change was originally derived for application in the field of geophysical imaging and has since found wide application in synthetic aperture radar (SAR). Like ISAM, SAR is a coherent imaging technique that employs transverse scanning and a spectral or time-of-flight measurement to gather range information. In fact, SAR and ISAM can be cast in the same mathematical framework [32], with standard radar being the direct analog of OCT. More broadly, the idea of computational imaging through Fourier-domain coordinate mappings can be found in fields including x-ray computed tomography [33, 34], diffraction tomography [35-37] and magnetic resonance imaging [38].

(3.3)Rigorous forward model

In this section a rigorous description of the physics of data acquisition is employed to derive an accurate forward model that is valid for arbitrary NA and distance from focus. Specifically, the forward model is formulated for both near and far from focus cases using a general description for the focused field. This description of the focused field is incorporated into the general statement of the forward model in Eq. (1.3).

An arbitrary propagating scalar field can be represented as an angular spectrum of plane waves [39]. With the plane wave coefficients $G(q_x, q_y)$, the field can be synthesized as

$$g(x,y,z,k) = \frac{i}{2\pi} \iint G(q_x, q_y, k) \exp\left\{ i\left[q_x x + q_y y + k_z(q_x, q_y) z \right] \right\} dq_x dq_y .\qquad (1.13)$$

This equation is a more general expression for the focused field than Eq. (1.4). The Weyl identity from Eq. (1.6) is a specific case of the angular spectrum representation of Eq. (1.13), for a spherical wave. Eq. (1.13) shows that for a fixed value of k the three-dimensional field is defined by a two-dimensional set of plane wave coefficients. The field in any two-dimensional plane thus defines the entire propagating field.

Focused beams can be described in the framework given in Eq. (1.13), e.g. for a Gaussian beam $G(q_x, q_y)$ is Gaussian. The relationship to Fourier optics is also clear as the transverse Fourier transform at any (x, y) plane is

$$\tilde{g}(q_x, q_y, z, k) = i2\pi G(q_x, q_y, k) \exp\left[ik_z(q_x, q_y)z\right]. \quad (1.14)$$

In addition to describing the angular spectrum of the field, the function $G(q_x, q_y)$ gives the form of the field on the exit pupil of the objective lens [40]. In this manner the objective lens determines the structure of the focused beam.

As suggested by the simplified derivation in Section 3.2, it is useful to take the forward model into the Fourier domain. Returning to Eq. (1.3), it can be seen that the backscattered field is expressed as a correlation of the scattering potential with the square of the focused field. Using basic properties of the Fourier transform (in particular for correlation, convolution and multiplication in each domain), Eqs. (1.2) and (1.3) can be written as

$$\tilde{S}(q_x, q_y, k) = \frac{k^2 |E_r(\omega)|^2}{4\pi^2} \int [\tilde{g} * \tilde{g}](-q_x, -q_y, z, k) \tilde{\eta}(q_x, q_y, z) dz, \quad (1.15)$$

where $*$ is the convolution operator over the transverse coordinates only.

The Fourier-domain data and the Fourier-domain sample are now related by a one-dimensional linear integral equation, rather than the three-dimensional integral equation seen in the spatial domain. However it is still necessary to specify the integral kernel $[\tilde{g} * \tilde{g}](-q_x, -q_y, z, k)$. Explicitly,

$$[\tilde{g} * \tilde{g}](q_x, q_y, z, k) = -4\pi^2 \iint G(q'_x, q'_y) G(q_x - q'_x, q_y - q'_y)$$
$$\exp\left\{i\left[k_z(q'_x, q'_y) + k_z(q_x - q'_x, q_y - q'_y)\right]z\right\} dq'_x dq'_y. \quad (1.16)$$

This expression simplifies considerably in certain asymptotic limits. Unsurprisingly, these asymptotic limits differ depending on whether in-focus or far-from-focus regions are considered.

For the in-focus case the magnitude of z is small and the product $G(q'_x, q'_y) G(q_x - q'_x, q_y - q'_y)$ dominates the convolution integral. For an unobscured objective, the field at the exit pupil is singly peaked and continuous so that $G(q'_x, q'_y)$ is also singly peaked and continuous. Consequently, the product

$G\left(q'_x,q'_y\right)G\left(q_x-q'_x,q_y-q'_y\right)$ is peaked around $\left(q'_x,q'_y\right)=\left(q_x/2,q_y/2\right)$. Expanding the integrand of Eq. (1.16) as a Taylor series about this point and retaining the first term results in the approximation

$$[\tilde{g}*\tilde{g}]\left(-q_x,-q_y,z,k\right)\approx-4\pi^2 H_N\left(q_x,q_y,k\right)\exp\left[i2k_z\left(\frac{q_x}{2},\frac{q_y}{2}\right)z\right], \tag{1.17}$$

where $H_N\left(q_x,q_y,k\right)$ is a function describing the in-focus transfer function of the instrument. Full details of this approximation and an expression for $H_N\left(q_x,q_y,k\right)$ can be found in [41].

Far from the focus, the magnitude of z is large and the exponential factor in Eq. (1.16) becomes highly oscillatory and the integrals can be evaluated using the method of stationary phase [29]. This method recognizes that the rapid oscillations will result in the integral cancelling to zero over the domain of integration, except at stationary points of the oscillation phase. Using Eq. (1.10) it can be shown that stationary points of the phase function $k_z\left(q'_x,q'_y\right)+k_z\left(q_x-q'_x,q_y-q'_y\right)$ occur when $\left(q'_x,q'_y\right)=\left(q_x/2,q_y/2\right)$. As a result, for regions far from the focus, Eq. (1.16) becomes

$$[\tilde{g}*\tilde{g}]\left(-q_x,-q_y,z,k\right)\approx-4\pi^2\frac{H_F\left(q_x,q_y,k\right)}{kz}\exp\left[i2k_z\left(\frac{q_x}{2},\frac{q_y}{2}\right)z\right], \tag{1.18}$$

where $H_F\left(q_x,q_y,k\right)$ is a function describing the out-of-focus transfer function of the instrument. As in the compact derivation from Section 3.2, the signal falls off as $1/z$.

A simplified forward model incorporating both the in-focus and out-of-focus cases can be obtained by combining Eqs. (1.17) and (1.18) with the exact forward model of Eq. (1.15), to give

$$\begin{aligned}\tilde{S}\left(q_x,q_y,k\right)&\approx k^2\left|E_r\left(\omega\right)\right|^2\int\frac{H\left(q_x,q_y,k\right)}{R(z)}\tilde{\eta}\left(q_x,q_y,z\right)\exp\left[i2k_z\left(\frac{q_x}{2},\frac{q_y}{2}\right)z\right]dz\\&=k^2\left|E_r\left(\omega\right)\right|^2 H\left(q_x,q_y,k\right)\tilde{\tilde{\eta}}'\left(q_x,q_y,-2k_z\left(\frac{q_x}{2},\frac{q_y}{2}\right)\right)\end{aligned} \tag{1.19}$$

where $H(q_x, q_y, k) = H_N(q_x, q_y, k)$ and $R(z) = 1$ for near-focus regions, and

$H(q_x, q_y, k) = H_F(q_x, q_y, k)$ and $R(z) = kz$ for far-from-focus regions. It has been shown [41] that the transition between these two regimes occurs at approximately one Rayleigh range, *i.e.*, when $|z| = \lambda / (\pi NA^2)$.

As shown previously in Eq. (1.9), the effect of the imaging system is reduced to a one-to-one relationship between the Fourier-domain data and the Fourier-domain object, although the Fourier domain object $\tilde{\eta}'(q_x, q_y, \beta)$ is here defined as the three-dimensional Fourier transform of $\eta(x, y, z)/R(z)$. The spherical-wave model used in the Section 3.2 only modeled low-NA out-of-focus regions accurately, and so did not address the near-focus or high-NA cases. However, it can be seen from the coordinate relationship in Eq. (1.19) that the same Stolt mapping also applies for both in-focus regions and at high NA.

(3.4)Inverse scattering procedure

The Stolt mapping present in the forward model gives a one-to-one, Fourier-domain relationship between the data and the object. This suggests a simple algorithmic procedure for inverse scattering. The algorithm can be summarized as;

1. Beginning with the complex interferometric signal $S(u, v, k)$, take the transverse Fourier transform to get the Fourier domain data $\tilde{S}(q_x, q_y, k)$.

2. Apply a linear filter, *i.e.* Fourier-domain multiplication of $\tilde{S}(q_x, q_y, k)$ and a transfer function, in order to compensate for the transfer function of the instrument $H(q_x, q_y, k)$. Note that the transfer function, and hence the filtering, depends on whether the scattering of interest is in the near- of far-from-focus zone. The instrument transfer function is usually relatively smooth, meaning that this step can often be omitted without significant detriment to the resulting image.

3. Re-map the coordinate space of $\tilde{S}(q_x, q_y, k)$ according to the Stolt mapping of Eq. (1.11) and Figure 4. For computational convenience resampling, *i.e.* interpolating the re-mapped data to a regular grid, can be employed.

4. Take the inverse Fourier transform to recover $\eta(x, y, z)/R(z)$, the attenuated object.

5. If required, the scattering potential $\eta(x, y, z)$ can be computed by multiplying by $R(z)$ to compensate for signal loss away from the focus.

Note that it may also be necessary to add preprocessing steps to account for material dispersion and compensate for phase instabilities in the instrument. Further details of ISAM processing, including its real-time implementation, are found in Section 4.4.

(3.5) Numerical simulations for a single scatterer

Numerical simulations provide a first step in validating the ISAM methods derived above. In the simulations presented here, a high-NA system is modeled using a vectorial model of high-angle focusing [40]. While not addressed in this work, it should be noted that vectorial fields have also been investigated in ISAM [41], with similar results to those shown here.

Results for the imaging of an out-of-focus on-axis point scatterer are shown in Figure 5. In these simulations a numerical aperture of 0.75 was used and light was collected between wavelengths of 660 nm and 1000 nm. Further explanation of this type of simulation can be found in [41]. The ISAM processing consisted only of the Fourier-domain mapping seen in Figure 4, and did not account for the transfer function of the instrument (see step 2 of the inverse scattering algorithm of Section 3.4).
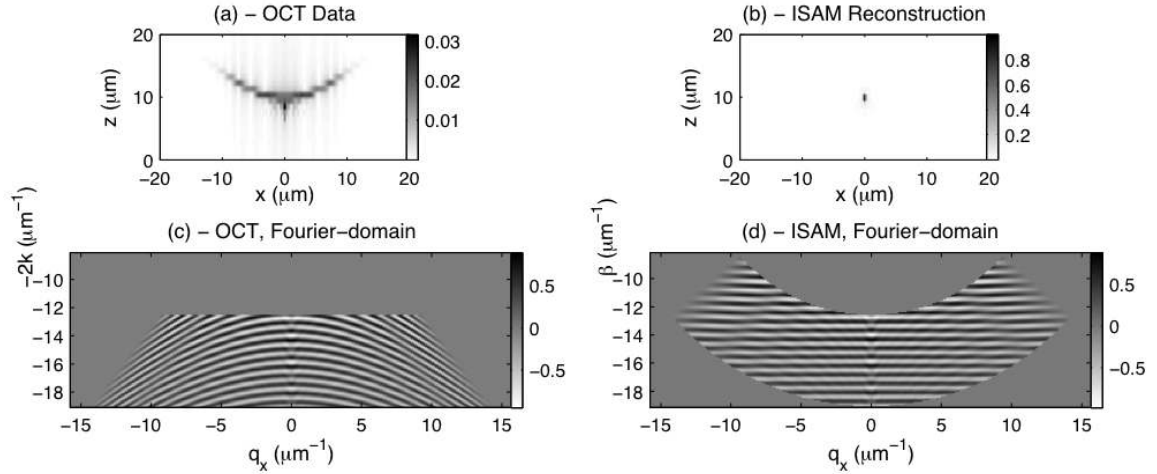
Figure 5: A simulated OCT image (a) of a point scatterer located at (0,0,10) μm and the real part of the three-dimensional Fourier transform of the image (c). ISAM processing takes the function seen in (c) to the reconstruction with real part plotted in (d). Taking the inverse Fourier transform of (d) results in the ISAM image seen in (b). Note that the two-dimensional plots shown are cross-sections of three-dimensional functions and that (a) and (b) display the magnitude of complex images. This figure is adapted from [32].

In Figure 5 it can be seen that out-of-focus blurring produces significant distortions in the OCT data. The point scatterer is extended laterally and has a curvature due to the curvature of the probing wave fronts. In the Fourier space of the object, an on-axis point should become a complex exponential with phase fronts perpendicular to the z axis. However in the measured OCT data, these Fourier phase fronts are curved. After ISAM processing is applied, straight parallel phase fronts are produced, as expected. The resulting in-phase superposition over all spatial frequencies, produces a sharp image of the point scatterer in the spatial domain, with the effects of defocusing removed.

(3.6)Alternate acquisition geometries

The results presented in the previous sections are derived for the standard confocal implementation of OCT and ISAM, with Cartesian lateral beam scanning in the x-y plane. However, other modalities can be addressed using a similar Fourier space resampling procedure. For example, in full-field ISAM [42] the sample is illuminated

with an axial plane wave $\exp(ikz)$ and the scattered light is focused onto an array detector, leading to the detection model $g(x-u, y-v, z, k)$. In this case, a one-to-one Fourier-domain forward model can be derived without approximation and the mapping

$$\beta = -k - k_z\left(q_x, q_y\right) \qquad (1.20)$$

applies. This coordinate mapping also appears in diffraction tomography. The solution of the inverse scattering problem via Fourier space resampling has also been described for full-field ISAM with partially-spatially-coherent illumination [43] and for a catheter-based, rotationally-scanned geometry [44].

(4)Experimental implementation and validation

(4.1)Phase stability and data acquisition requirements

Phase stability is a primary requirement to perform ISAM on an OCT system. Although phase variations may be nearly imperceptible in a magnitude OCT image, phase stability is important to many OCT studies that depend on the measurement of complex signals. For instance, phase stable measurements are required for Doppler OCT [45], phase microscopy [46-49], polarization sensitive OCT [50], coherent averaging [51], and spectroscopic OCT [52, 53]. In ISAM, the three-dimensional Fourier transform of the object $\tilde{\tilde{\eta}}(q_x, q_y, \beta)$ is obtained through resampling of the experimentally derived complex array $\tilde{S}(q_x, q_y, k)$. Implicit to the resampling scheme is the assumption of a precise and predictable relationship between the components of $\tilde{S}(q_x, q_y, k)$. Precise recovery of the spatial frequency profile for scatterers located away from the beam focus is disrupted by random phase fluctuations during data acquisition.

Phase stability requirements on the instrument can be elucidated by consideration of the data acquisition. Typically, two-dimensional raster scanning of a Gaussian beam interrogates each scattering location within the object. As described in Section 2, lateral beam scanning across a point scatterer situated away from focus results in contributions to the data at many scan points (u, v). Image reconstruction from these data therefore requires phase-stable acquisition during the "interrogation time" corresponding to the

length of the synthetic aperture for any given scatterer. The interrogation time at any given location (x_0, y_0, z_0) depends on its distance from focus and the NA of the beam (see Figure 2). When beyond about one Rayleigh range, the interrogation time scales linearly with both distance from focus, and the beam NA. The desired NA and depth-of-field determine the maximum interrogation time, and thus place requirements on the phase noise spectrum of the instrument.

Two main sources of phase noise can be identified in the instrument. Firstly, environmental vibrations and thermal drifts produce axial fluctuations in the differential pathlength between the reference and sample arms. Secondly, imprecise lateral scanning due to mechanical jitter can cause deviations from the expected iso-phase contours in $\tilde{S}(q_x, q_y, k)$. For the first case, phase noise is spread uniformly over all q, whereas in the second case, instabilities in lateral beam scanning are more significant at higher NA and near the beam boundary where the phase slope $\partial\phi / \partial x|_k$ is greatest (see Figure 2). Mechanical instabilities during lateral scanning thus limit the bandwidth that produces predictable interference during reconstruction. A general rule of thumb, given that random phase shifts of $\Delta\phi = \pm\pi$ produce a maximal change in interference, it is desirable to maintain phase fluctuations below $\lambda / 4$ over the length of the depth-dependent synthetic aperture.

To date, ISAM has been performed on spectral-domain OCT systems. Simultaneous acquisition of $S(x, k)$ on the spectrometer facilitates phase registration over k, while TD-OCT, acquired through reference arm scanning, is prone to the effects of mechanical jitter. In addition, spectral-domain acquisition enables A-scan acquisition rates on the order of tens of kilohertz, thus minimizing scatterer interrogation time during lateral scanning. At numerical apertures around 0.1, the scanning and detection hardware for Fourier-domain OCT will produce relatively phase-stable two-dimensional (2D) imagery. However, when performing three-dimensional (3D) imaging, the acquisition time generally increases to a point where phase noise can again become an issue. Recent developments in swept-source technology, such the high-speed Fourier domain mode-

locked laser, can perform phase-sensitive imaging at speeds unattainable by spectrometer-based systems [54].

(4.1.1)Hardware solutions for phase registration

Phase stable data acquisition can be achieved via a number of methods. In general, phase noise can be mitigated by instrument design – incorporating higher speed acquisition, vibration isolation, and minimizing fiber lengths to reduce thermal drifts. However the optimal solution largely depends upon the practical feasibility for the specific experimental geometry or application, and cost of its implementation. For example, obtaining the level of vibration isolation required for high-NA systems may be cost prohibitive. Several alternative hardware solutions may be considered, such as the use of a phase reference, a free-space or common path design or a feedback control loop to compensate for phase fluctuations in real-time.

A phase reference directly coupled to the sample has been shown to mitigate the ill effects of differential phase fluctuations between reference and sample arms [48], enabling the observation of cell membrane dynamics. By referencing the heterodyne phase of the sample to that of a coverslip, upon which the cells were mounted, displacement and velocity sensitivities of 3.6 nm and 1 nm/s were achieved. For bulk samples a coverslip can be placed upon the sample, and when appropriately aligned, can also reduce strong surface reflections from the sample. This hardware solution is used in conjunction with algorithms to compensate for phase fluctuations in the system. Section 3.1.2 describes a digital algorithm utilizing the response from such a phase reference to correct phase fluctuations.

Free-space or common-path interferometer designs are often employed when low differential path length variations are required [46, 47, 55]. Placing a beamsplitter in the free-space optical section of the sample arm essentially forms a free-space Michelson interferometer within the sample arm probe. A common-path design may be obtained by utilizing the phase reference coverslip mentioned above as the "reference arm reflection". Virtually all phase noise in the system is common mode between the reference and sample optical fields, resulting in sub-nanometer displacement sensitivities [47].

Other sophisticated hardware solutions exist, such as the use of a feedback control loop in conjunction with a fiber stretcher or piezo-electric modulator [56, 57]. In these setups, fringes are counted or tracked and the reference path length is adjusted to compensate. However, these physical compensators may only be moved with limited speed and accuracy, and may be most useful in the context of large drifts over a few microns.

(4.1.2) Post-processing methods for phase registration

Post-processing techniques compensate for phase noise during data acquisition through alignment of the complex A-scans in time-domain. This alignment can be carried out by using the phase reference mentioned in Section 3.1.1, or via direct cross correlation of the complex A-scans based on scattering signals from the sample.

(4.1.2.1)Phase reference technique

In the phase reference technique, phase and group delay values are calculated for each A-scan to compensate for the differential variations in optical path length. Because the coverslip signal $S_c(k)$ corresponds to a single reflection, it can be modeled as $S_c(k) = A(k)e^{i\phi(k)}$, where the phase function $\phi(k) = \phi_0 + kd$, where ϕ_0 is an arbitrary phase and d is the true position of the surface where the reference reflection occurs. Due to the relative motion of the sample, the actual phase will differ from this model giving $\arg[S_c(k)] = \phi'(k)$. By multiplying the axial scan data $S(k)$ by the correction factor $e^{i[\phi(k)-\phi'(k)]}$, the phase of the axial scan can be adjusted to place the reflection at its true known position d.

The phase $\phi'(k)$ is modeled as a Taylor series around a center frequency k_0:

$$\phi'(k) = \phi'(k_0) + (k - k_0)\frac{\partial\phi'}{\partial k}\bigg|_{k=k_0} + \dots \qquad (1.21)$$

To utilize this model, the value of $\partial\phi'/\partial k\big|_{k=k_0}$ from the data function $\phi'(k)$ must be estimated. Since the function $\phi'(k)$ is wrapped to the range $-\pi$ to π, any 2π

discontinuities need to be removed before calculating the derivative. Utilizing the unwrapped function $\phi_w(k)$, the estimate then becomes

$$\left.\frac{\partial \phi'}{\partial k}\right|_{k=k_0} \approx \frac{\phi_w(k_2)-\phi_w(k_1)}{k_2-k_1}, \tag{1.22}$$

where $k_1 < k_0 < k_2$, with the frequencies k_1 and k_2 chosen to span the illumination spectrum (typically with k_1 and k_2 corresponding to the frequencies at which the power spectral density is half of that at the peak).

Once $\phi'(k_0)$ and $\left.\partial\phi'/\partial k\right|_{k=k_0}$ are known, the empirical $\phi'(k)$ can be computed, and the corrected axial scan spectrum $S'(k) = S(k)e^{i[\phi(k)-\phi(k')]}$ found. This corrected axial scan data will be modified such that the position of the reference reflection is always at the same location on the axial scan, thus removing differential pathlength fluctuations between the reference and sample arm.

Figure 6a shows the real part of the complex analytic OCT signal from a single reflection of a coverslip where there is a phase drift. Figure 6b shows the same data after running the phase correction algorithm. Figure 6c and d show plots of the phase and group delay correction factors calculated from the original data. Refinements to this method could utilize higher order terms of the series for $\phi'(k)$, which would account for instrument dispersion as well as motion.

(a) Original Coverslip   (b) Corrected Coverslip

$$\phi'(k_0)$$

$$\left.\partial\phi'(k_0)\middle/\partial k\right|_{k=k_0}$$
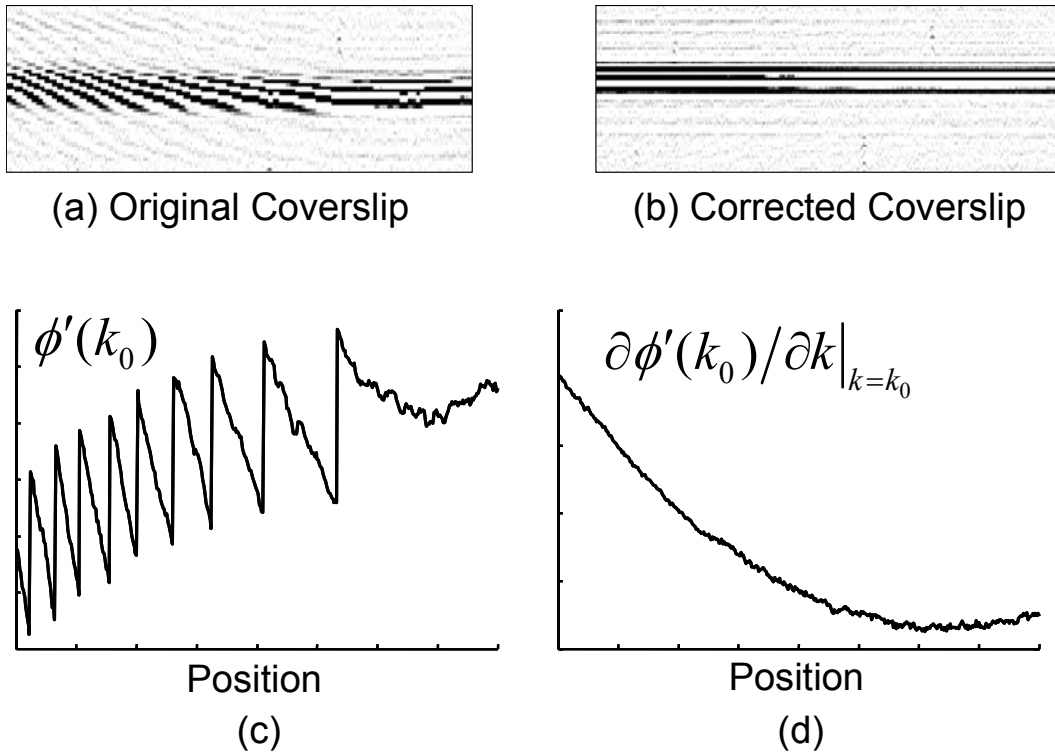
Position   Position

(c)   (d)

Figure 6: Real part of the complex OCT signal for a single reflector for (a) the OCT data and (b) the phase-corrected OCT data. The correction factor calculated from the original data for the (c) phase drift and (d) group delay drift. This figure is adapted from Ref. [58].

The impact of this phase correction algorithm on the quality of ISAM reconstruction can be evaluated through imaging of a gel-based tissue phantom containing TiO_2 scatterers. Three-dimensional imaging was performed over 800 µm × 800 µm (transverse) × 2000 µm (axial) at 4 frames/s, on a system with 800 nm central wavelength and 100 nm bandwidth, and a sample arm NA of 0.05. Cross-sectional images (400 × 1024 pixels) oriented along the slow y-axis scan (250 ms between A-scans), are shown in Figure 7. It can be seen that the OCT images are not noticeably different after the phase correction procedure. However, the ISAM image in Figure 7b shows a dramatic improvement in away-from-focus resolution after phase correction.
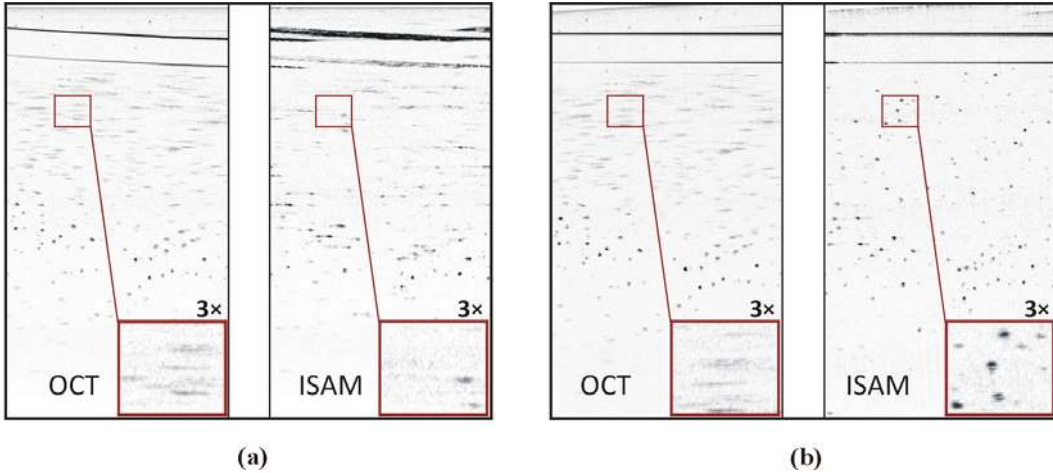
Figure 7: Cross-sectional OCT and ISAM images of a gel-based tissue phantom containing scattering TiO$_2$ particles, processed (a) without phase correction, and (b) with phase correction. The images are extracted from a 3D dataset, where the transverse dimension shown is oriented along the slow *y*-axis scan. Phase correction was applied to the entire 3D dataset. Image dimensions are 800 μm (transverse) × 2000 μm (depth).

(4.1.2.1)Cross-correlation technique

The cross-correlation technique, based on scattering signals within A-scans, may be employed when it is impractical or undesirable to use a phase reference coverslip, or to correct residual phase fluctuations due to motion between the coverslip and sample. Cross-correlation can be utilized when there is adequate overlap between adjacent A-scans, and the phase fluctuations are slow compared to the A-scan rate. Cross-correlation methods have previously enabled coherent spectral averaging, leading to improved OCT system sensitivity [51].

The algorithm finds the cross-correlation of a pair of time-domain scans by multiplying their real-valued spectra in the Fourier domain. This operation results in a dataset that has a maximum peak at an offset corresponding to the drift between the A-scans. The corresponding phase correction can then applied to the complex time-domain signal.

(4.2)Three-dimensional ISAM of tissue phantoms

In order to test the performance of ISAM reconstruction it is useful to work with a sample in which the density and complexity of the structure can be regulated, and the point-spread function of the system can be tracked. Tissue phantoms consisting of discrete point scatterers represent an ideal sample for such investigations since the density and particle size can be controlled to study different regimes of operation. Three-dimensional imaging was performed on tissue phantoms consisting of TiO_2 scatterers with a mean diameter of 1 μm suspended in silicone. Imaging was conducted on a system with 800 nm central wavelength and 100 nm bandwidth. The sample arm numerical aperture of 0.05 provided a confocal parameter (depth-of-focus equal to twice the Rayleigh range) of 239 μm. Figure 8 presents side-by-side visualization of the OCT and ISAM datasets. It can be seen that the OCT dataset begins to show blurring at a distance of 240 μm from focus, with increased blurring further from focus. In contrast, the ISAM reconstruction provides spatially-invariant resolution over a depth exceeding nine Rayleigh ranges.
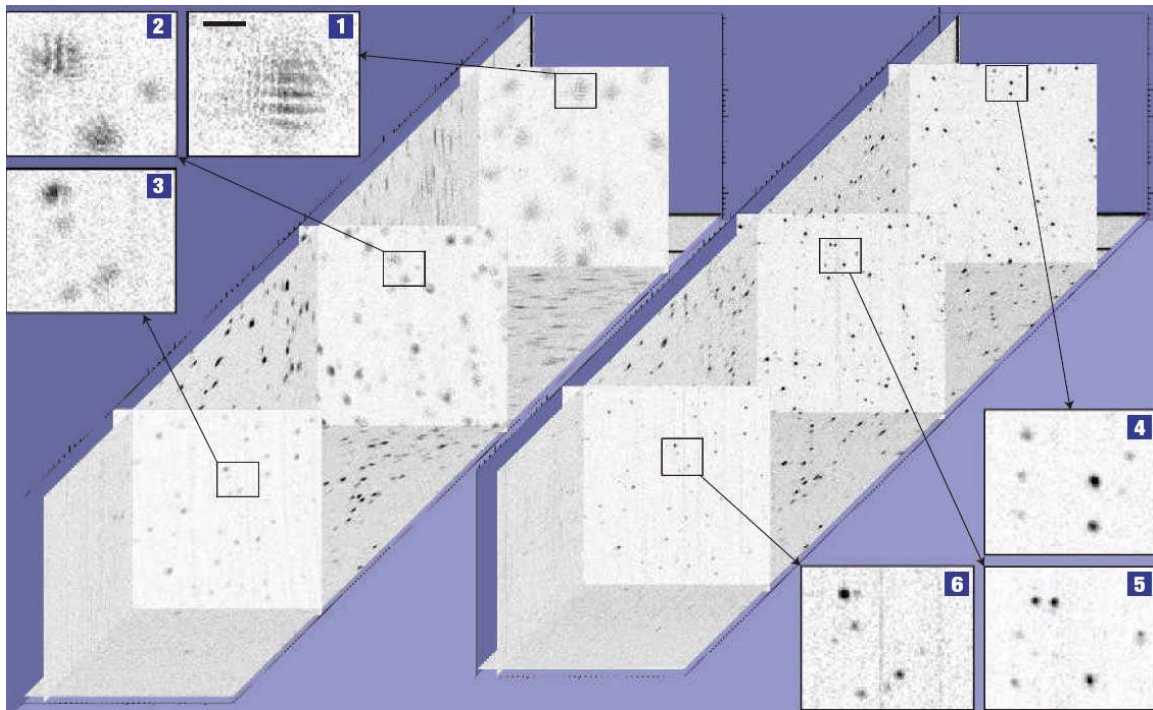

Figure 8: Three-dimensional OCT (left) and ISAM (right) images of TiO_2 phantoms. The three *en face* planes in each dataset correspond to (1) z = 1100 μm, (2) z = 475

μm and (3) $z = $ -240 μm, where $z = 0$ μm is the focal plane. Figure reprinted with permission from [3].

(4.3) Cross-validation of ISAM and OCT

While good agreement is obtained between *en face* OCT and ISAM images near the beam focal plane, it is of interest to determine whether ISAM reconstructed *en face* planes far from focus provide equivalent images to physically moving the beam focus to that plane.

Cross-validation of ISAM and OCT was achieved by performing ISAM and OCT imaging in a TiO_2-doped tissue phantom at two separate focal plane depths (Figure 9). Three-dimensional ISAM and OCT datasets were obtained with the focus fixed 450 μm below the *en face* images shown in Figure 9a and b. The sample was then moved 450 μm so that 3D-OCT could be captured again, with the same *en face* plane now at focus. Accounting for the index of refraction in silicone, the in-focus OCT image was co-registered with the corresponding computationally reconstructed ISAM image (Figure 9b and c).
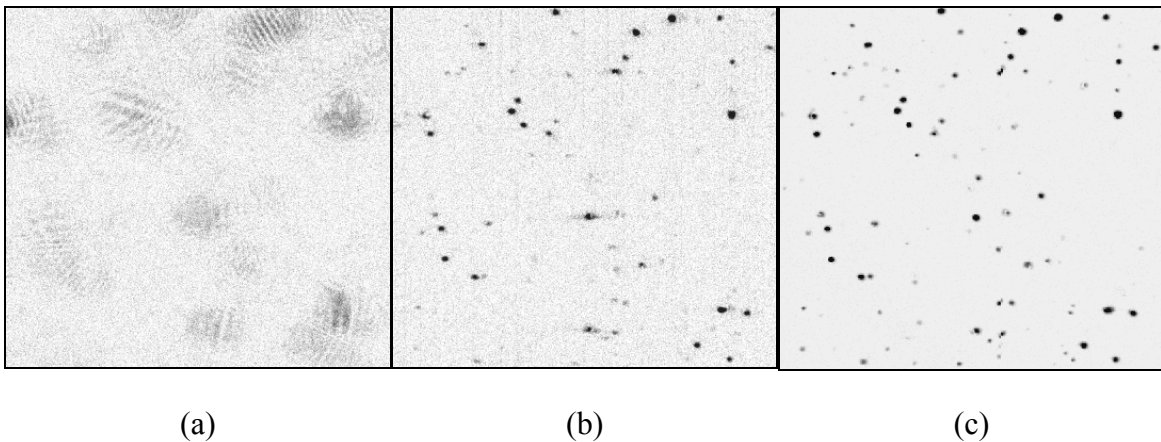

| (a) | (b) | (c) |

Figure 9: (a) *En face* OCT of a plane 450 μ m above the focal plane. (b) ISAM reconstruction of the same *en face* plane. (c) *En face* OCT with the focal plane moved to the plane of interest in (a). The field of view in each panel is 360 μ m by 360 μ m.

The out-of-focus OCT image in Figure 9a shows fringe patterns resulting from simultaneous illumination of two (or more) point scatterers, and the resulting interference of their scattered optical fields. The ISAM reconstruction of this plane in Figure 9b shows that these interference fringes are correctly resolved as multiple point scatterers, and good agreement is observed with the in-focus OCT image of Figure 9c. While the resolution observed in the ISAM and in-focus OCT images are comparable, the SNR of the ISAM image is reduced. This degradation of SNR away from the focal plane is discussed further in Section 4.5.

(4.4)ISAM processing and real-time implementation

Real-time imaging is important for clinical applications that require immediate feedback, and for monitoring transient dynamics of biological systems [59-62]. OCT acquisition speed has increased dramatically with the development of new spectral-domain and swept-source imaging systems [54, 63], and in order fully utilize these acquisition speeds, computations need to be streamlined and parallelized. Commercialization of the technology for medical and research applications has accelerated the development of real-time OCT processing and visualization software. Although ISAM reconstruction is more computationally intensive than SD-OCT processing, real-time 2D ISAM reconstruction has been demonstrated on a personal computer with two 3.0 GHz Intel Xeon processors, at frame rates of 2.25 frames per second for 512×1024 pixel images [64]. The general processing steps for offline 2D ISAM reconstruction are summarized below, along with the modifications made to achieve real-time processing. At this stage the reader is cautioned that while 2D ISAM reconstruction may produce significant apparent resolution improvements away from focus, it is prone to blurring artifacts from out of plane scatterers, and that full 3D processing is required for accurate object reconstruction. That is, 2D ISAM sharpens the features in the image, but features from adjacent planes contribute and those contributions increase with distance from focus.

The general processing steps for reconstructing 2D images are presented in Figure 10a. The prime variables ω', k', and t' denote upsampled arrays of optical frequency, optical wavenumber and time, and the double prime t'' denotes an extra, upsampling

step. The hat $\hat{S}$ is used to denote phase corrected data. Modifications to the general algorithm for real-time implementation [64] are summarized in Figure 10b.
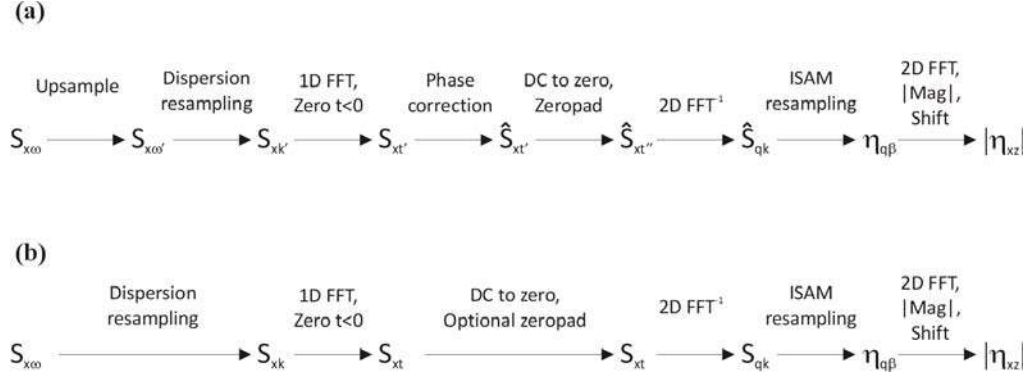

Figure 10: (a) General processing steps for 2D reconstruction, and (b) modified processing steps for real-time 2D reconstruction [64].

ISAM reconstruction requires two primary resampling operations and Fourier transforms to switch between the time and frequency domains. First is the resampling of $\omega' \rightarrow k'$, which also corrects mismatched dispersion between the sample and reference arms, *i.e.*, dispersion relations more complex than Eq (1.1) can be accounted for. The re-indexing array i_n for this step is given by

$$i_n = n + \beta_2 \left(\frac{n}{N} - \omega_{ctr} \right)^2 + \beta_3 \left(\frac{n}{N} - \omega_{ctr} \right)^3, \tag{1.23}$$

where N is the array size, ω_{ctr} is the center frequency, and n is an integer between 0 and N-1 [25, 26]. Eq (1.23) is a coordinate remapping, accounting for dispersion up to third order. Second is the ISAM Fourier space resampling from $k \rightarrow \beta$, which transforms from optical wavenumber k to longitudinal spatial frequency β. Typical SD-OCT processing is completed after computing $|S_{xt}|$, whereas ISAM processing requires two extra 2D FFTs and a further resampling step.

Upsampling plays an important role to minimize noise introduced by resampling in the final OCT and ISAM datasets. The two resampling (interpolation) steps have the effect of increasing the apparent bandwidth of the data, which in turn manifests as noise in $S_{xk'}$ and $\hat{S}_{qk}$ if the resampled grid is not sufficiently dense. Periodic-sinc interpolation

of $S_{x\omega}$ by a factor of two is often sufficient, however reconstruction quality may benefit from higher factors depending on the noise performance of the chosen interpolator. Similarly, upsampling of $\hat{S}_{qk}$ (zero padding of $\hat{S}_{xt'}$) can be performed to increase phase precision during ISAM resampling, or omitted to optimize processing speed. A nearest neighbor interpolation requires a minimal amount of computation, while a weighted sinc interpolation requires $O(N)$ operations per sample [65]. The cubic B-spline interpolator has a reasonable frequency response and uses only 4 multiply operations and 3 add operations to compute each interpolated point [64]. Other band-limited interpolators that could be used include prolate-spheroidal, hamming, and raised cosine. The phase correction step mitigates the effects of phase noise during data acquisition – details of algorithms used can be found in Section 4.1.2.

For real-time implementation, the two main dispersion and ISAM resampling steps can be performed using pre-computed tables of indices, where speed is further optimized by using the integer part of the computed indices, effectively employing nearest neighbor interpolation. Phase correction can be neglected for 2D ISAM images if the acquisition speed, and lateral scanning repeatability of the system is sufficient to maintain phase stability over the extent of the depth-dependent synthetic aperture. Upsampling of the data can be omitted to maximize speed, albeit with lower SNR in the reconstruction.

Most of the operations in ISAM reconstruction can be implemented using parallel processing code and hardware architectures. Therefore, additional computational hardware, such as multi-core CPUs or graphic processing units (GPUs), may be used to speed up the computations further, and bring real-time 3D ISAM reconstruction within reach. This will also address bleed-through artifacts present in 2D reconstruction caused out-of-plane scatterers.

(4.5) Practical limitations

ISAM shares many of the practical limitations present in OCT, such as the assumption of single scattering, attenuation of signal-to-noise ratio (SNR) away from focus, and light extinction within the sample. Vignetting occurs in both ISAM and OCT,

although its effects are not typically discernable in OCT images. Phase noise in the instrument can impose additional limitations on the quality of the ISAM reconstruction, particularly at high NA.

The assumption of single scattering, *i.e.*, the first Born approximation, is used to linearize the inverse scattering problem. When this assumption breaks down, the accuracy of both ISAM and OCT is degraded. Indeed, the penetration depth in OCT is often limited by the collection of multiple scattering, which can dominate over the singly scattered component at large depth [9, 66, 67].

Attenuation of SNR with distance from focus is governed by the beam and confocal acquisition geometry. At out-of-focus depth z, the SNR is reduced by a factor of $1/R(z)$, where $R(z)$ is the number of Rayleigh ranges from focus [32]. Although ISAM does not require longitudinal scanning of the focus to achieve uniform resolution, it may be possible to combine measurements from a variety of focal depths to improve SNR. Since the method provides a quantitative reconstruction uniform in the object space from data acquired at each fixed depth, multiple scans, even those with foci many Rayleigh ranges away from each other, may be combined, for example with a least squares or maximum likelihood approach.

Vignetting is more apparent further away from focus, and near the edge of the lateral field of view. It occurs for scatterers near the edge of the field, since they are probed by a truncated synthetic aperture. This results in a reduction of signal amplitude and an attenuation of high lateral spatial frequency components. Higher NA and distance from focus increases the synthetic aperture length and therefore the effects of vignetting.

Phase noise of the instrument can reduce the degree of coherent interference obtained during resampling, and therefore the SNR of the reconstructed data. As discussed in Section 4.1, the phase noise of the instrument impacts on the maximum interrogation time (corresponding to the extent of the synthetic aperture) and therefore the imaging NA and required depth-of-field cannot be chosen arbitrarily. In addition, at high NA, the effects of lateral scanning instabilities produce greater phase noise for the acquisition of high lateral spatial frequencies. This may disrupt the coherent

superposition of these high frequency components during reconstruction, degrading the performance away from focus.

(5)Clinical and biological applications

Many biological and clinical application areas of OCT could benefit from ISAM imaging, in particular when higher resolution and field-of-view increases the diagnostic value of images. Several studies investigating the impact of axial and lateral resolution have found that higher resolution provided enhanced diagnostic information, but that high lateral resolution did not permit clear visualization of important structures away from focus [68-70]. Spatially invariant ISAM reconstruction of the sample, offering both high lateral resolution and extended depth-of-field, could significantly enhance the diagnostic capabilities of OCT. Important biological and clinical application areas, and how they may benefit from ISAM, are discussed below.

(5.1)Optical biopsy

Excisional biopsy and subsequent histopathological analysis is currently the gold standard for diagnosing neoplasia. The main drawback of this technique is sampling errors, which can occur from inaccurate selection of neoplastic tissue during excision, or during analysis of a sample with both normal and neoplastic tissue in the pathology laboratory. Inaccurate excision is the result of imperfect methods for detecting and excising neoplastic areas of tissue, while the time consuming nature of histopathology limits the number of tissue sections that are analyzed routinely. Both can increase the false negative rate of diagnosis. One of the key areas that OCT is being applied to is performing an 'optical biopsy' or for optical biopsy guidance [71, 72]. Optical biopsy refers to the detection of neoplasia *in vivo*, while the capability of identifying suspicious areas can be used to guide physical excision of tissue. Three-dimensional, high-resolution imaging combined with a large depth-of-field could significantly increase the diagnostic information available for optical biopsy. Visualization and analysis of 3D volumetric data with spatially-invariant resolution could further reduce sampling errors.

Three-dimensional imaging of resected human breast tissue was performed and compared to histology images, demonstrating the extended depth-of-field provided by

ISAM. Imaging was performed system on a system with 800 nm central wavelength and 100 nm bandwidth, with a focused beam numerical aperture of 0.05. Figure 11 presents the volumetric ISAM rendering and selected *en face* sections from near and far from focus. The *en face* ISAM sections are compared to corresponding OCT and histological sections. While the ISAM and OCT sections in-focus show similar information to histology images, the away-from-focus resolution improvements of ISAM are evident, providing a more accurate representation of the tissue structure.
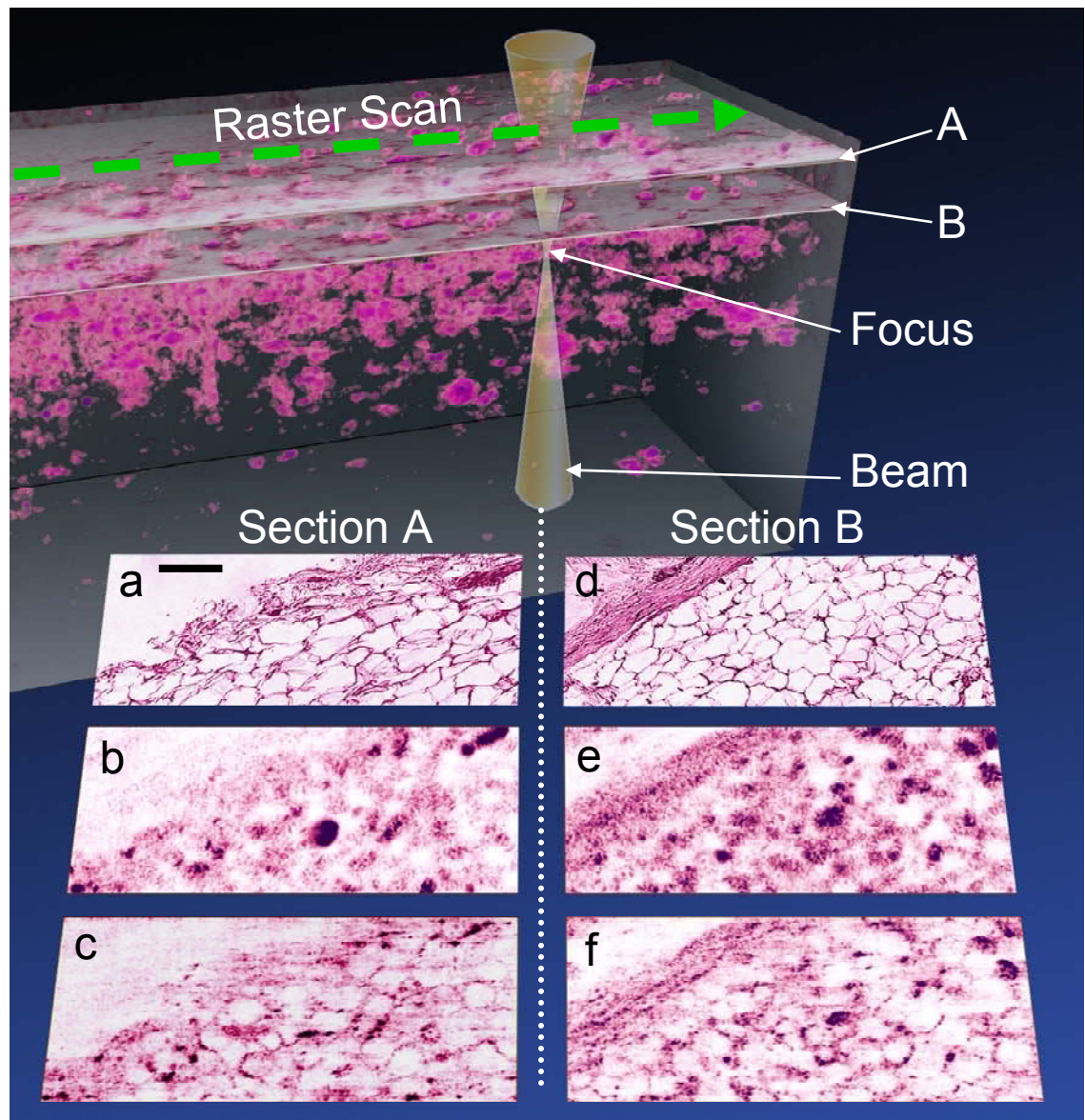

Figure 11: Resected human breast tissue imaged with Fourier-domain interferometry. The beam is scanned in the geometry shown at the top. *En face*

images are shown for depths located at 591 μm (Section A) and 643 μm (Section B) above the focal plane. (a,d) Histological sections show comparable features with respect to the (b,e) OCT data and (c,f) the ISAM reconstructions. The ISAM reconstructions resolve features in the tissue which are not decipherable from the OCT data. This figure is adapted from Ref. [3].

The combination of ultrahigh axial resolution [73] with ISAM presents an opportunity for unprecedented 3D visualization of turbid tissue, bringing cellular-level resolution over a large depth-of-field within reach. As a result, significantly more information regarding the tissue may be extracted without increasing the measurement time or scanning the focal plane. Further study is required to investigate the capability of ISAM to distinguish between normal and neoplastic tissue, and to assess its *in vivo* diagnostic capabilities.

(5.2) Surgical guidance

The detection of tumor margins is important for the complete removal of tumor tissue. For example, positive or undetermined margins in excised breast tissue samples are correlated with significantly higher rates of residual cancer [74]. The evaluation of margin status during surgery motivates research on intraoperative OCT imaging of resected tissue [75], as well as direct imaging of the surgical field [18]. The sample arm of such systems can be implemented as a handheld or endoscopic probe, or incorporated into a surgical microscope. Handheld or endoscopic probes can include an optical window for contact with the tissue, allowing precise placement of the focus, which can also act as a phase reference for ISAM. During open surgery it is desirable for the surgeon to have access to the surgical field, suggesting a non-contact imaging geometry. For this geometry, precise placement of the focus relative to the sample surface is often difficult to obtain due to surface topography of the tissue. With the extended depth-of-field obtained with ISAM only coarse placement of the focus is required. This advantage is demonstrated through intraoperative imaging, performed on a portable OCT system, with a 1310 nm central wavelength and an 80 nm bandwidth, and a focused beam numerical aperture of 0.1.

Figure 12 presents real-time intraoperative imaging of tissue excised during a thyroidectomy procedure. Follicular structure that is typical of the thyroid is seen in both the OCT and ISAM images. However, due to the orientation (tilt) of the tissue surface, only a subset of the OCT image (about the strong surface signals) is in focus, while the real-time 2D ISAM reconstruction is able to resolve tissue morphology throughout the image. In particular boundaries between high and low scattering regions are resolved.
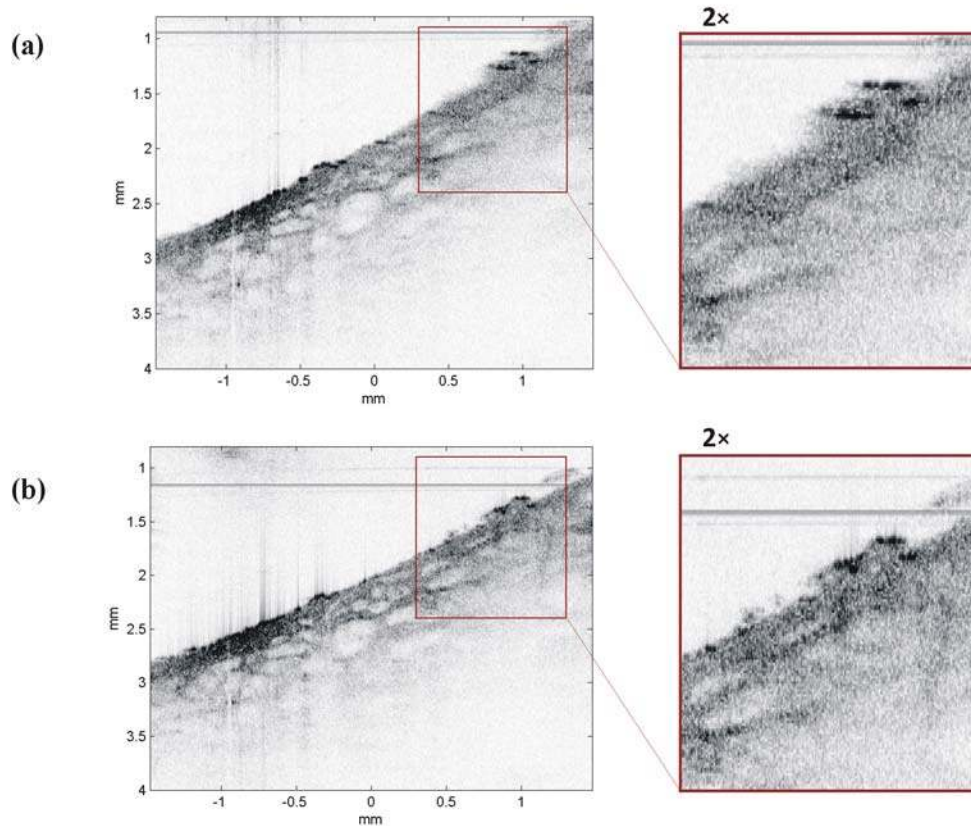

Figure 12: Intraoperative imaging of human tissue excised during a thyroidectomy procedure. (a) OCT image and (b) real-time 2D ISAM reconstruction.

Imaging of the margins of excised human breast tissue was performed during a lumpectomy procedure (see Figure 13). Due to the irregular tissue topography and time constraints inherent with intraoperative imaging, precise positioning of the focus was not achieved. The current form of the real-time algorithm does not permit dynamic adjustment of the focus depth during image acquisition, and as a consequence, the real-time 2D ISAM image (not shown here) did not provide significantly better resolution. However the post-processed image shown in Figure 13b, demonstrates that

the tissue structure can be brought into focus by adjustment of the focus depth used by the algorithm. With further work, the real-time algorithm can be adapted to dynamically compensate for imprecise focus placement, and provide automated computational focusing.
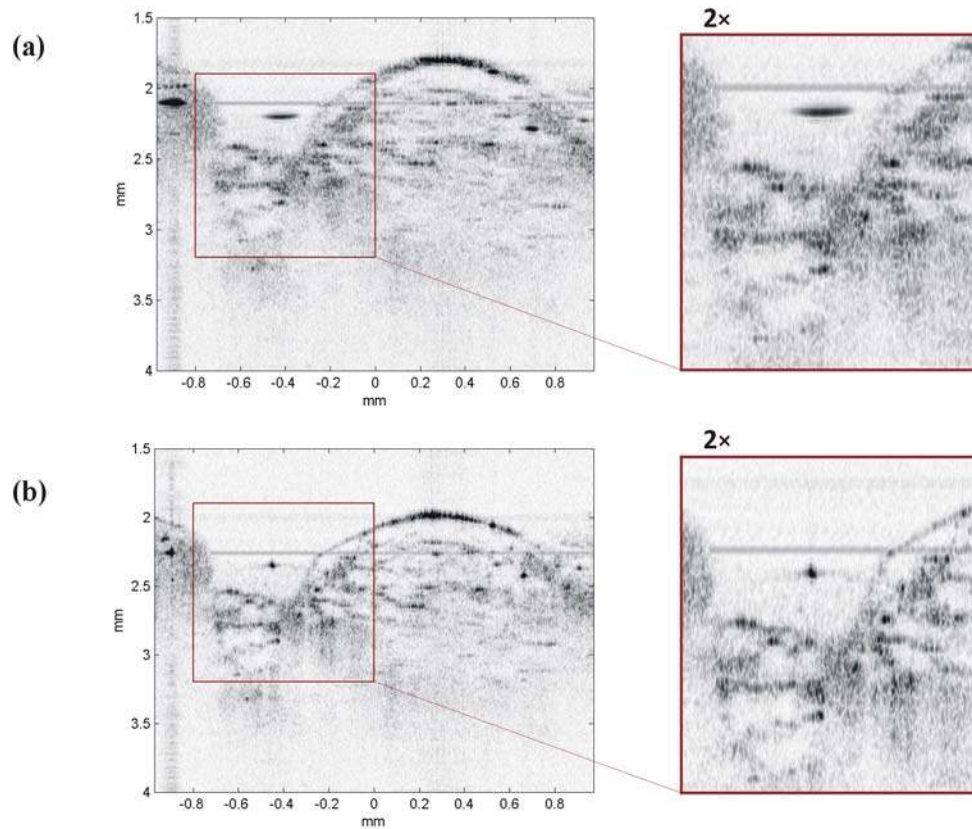

Figure 13: Intraoperative imaging of human breast tissue excised during a lumpectomy procedure. (a) OCT image and (b) post-processed 2D ISAM reconstruction.

Tolerance to surface topography and imprecise placement of the focus provides flexibility for use during open surgery, or assessment of margin status of resected tissue. This could enable the surgeon to remove a higher percentage of cancerous tissue, and thereby reduce the rate of residual cancer. Another related procedure for which ISAM could be employed is the intraoperative screening and detection of abnormalities in sentinel lymph nodes [76]. This has the potential to reduce the number of nodes removed and thereby reduce the incidence of lymphadema, a life-long complication associated with the disruption of normal lymphatic drainage. For all of these proposed application

areas, further work is required to investigate the sensitivity and specificity of cancer detection with ISAM.

(5.3)Imaging tumor development

Traditional diagnosis of neoplastic changes is based on cellular features such as atypia of cell nuclei, accelerated rate of growth, and local invasion. Thus the pursuit of cellular imaging is motivating new developments in optical sources for ultrahigh resolution OCT, with axial resolutions on the order of 1 μm [73, 77]. In contrast, lateral resolution can be up to an order of magnitude larger to maintain a reasonable depth-of-field in cross-sectional images. The combination of ultrahigh axial resolution with high-NA ISAM has the potential to significantly increase the available diagnostic information by enabling isotropic, ultrahigh resolution.

Evaluation of the diagnostic capabilities of ultrahigh resolution ISAM can be conducted in the laboratory using tissue scaffolds. This could also suggest new ways that ISAM could be used in the clinical setting, as well as provide valuable data addressing the fundamental question of how tumors grow and spread. These studies could be extended to *in vivo* monitoring of tumor development in animal models. Induction of tumors in the dorsal skin-flap window of a rodent [78] represents a methodology that may be well suited to ultrahigh resolution ISAM imaging. In contrast to histopathology, where tissue excision provides a 'snapshot' of tissue, ISAM could be used to monitor tumor development over time within the same animal.

(6)Conclusions and future directions

ISAM is a computed imaging technique that quantitatively reconstructs the three-dimensional scattering object using broadband coherent microscopy. The solution of the inverse problem, implemented via Fourier space resampling allows reconstruction of areas typically regarded as out of focus in OCT. The Fourier-domain resampling employed in ISAM is physically motivated by the forward model for data acquisition and results in a quantitative estimate of the scattering potential. While ISAM shares many of the advantages and limitations present in OCT, its spatially invariant resolution obviates the perceived trade-off between transverse resolution and depth-of-focus present in OCT.

It is worth addressing a common misconception. ISAM is inverse scattering, where a reconstruction of the entire three-dimensional sample is obtained. ISAM is not refocusing. In refocusing, the focal plane is moved computationally, causing some features to be defocused while others are focused. Refocusing may be accomplished from a simple 2D hologram and the result is still 2D, while reconstruction such as ISAM requires a 3D (or higher dimensional) dataset to obtain a 3D reconstruction.

Experimental implementation of ISAM has been achieved through high-speed spectral-domain acquisition, and techniques for obtaining phase registered 3D datasets. Imaging of tissue phantoms has demonstrated spatially invariant resolution up to nine Rayleigh ranges from the focus, and cross-validation of ISAM with OCT was successfully performed. The discussion of ISAM processing emphasized the impact of key steps on reconstruction quality, such as phase correction, material dispersion correction, and upsampling. Modifications for real-time 2D processing achieved frame rates of 2.25 frames per second for 512×1024 pixel images.

Imaging of human tissue demonstrated extended depth-of-field imaging, providing more accurate representation of tissue morphology. Clinical applications where ISAM imaging could add significant value include optical biopsy and surgical guidance. Intraoperative imaging was demonstrated with a portable OCT system incorporating ISAM. The computational focusing capability of ISAM relaxes the requirement of precise focus placement within the tissue, providing greater flexibility when imaging tissue with irregular topography.

Future work on ISAM spans the range from theoretical modeling, to development of optical instrumentation and software processing, to clinical and fundamental biological studies. For example, modeling of light scattering within the sample is feasible when the structure of the sample is known. Thus reconstruction of the object structure with ISAM could allow extended modeling of scattering beyond the first Born approximation. Development of high-NA instrumentation for high isotropic resolution, presents challenges and opportunities, such as computational compensation for optical aberrations. High-NA ISAM combined with ultrahigh resolution sources promises cellular-level resolution, suggesting the application to fundamental laboratory studies on tumor

development. Parallelization of 3D ISAM algorithms for hardware architectures such as a GPU could add significant clinical diagnostic value by enabling high-resolution, real-time 3D visualization of tissue. Finally, clinical studies on the sensitivity and specificity of ISAM to diagnose diseases such as cancer will ultimately determine what role ISAM plays in the future of health care.

References

1. Huang, D., et al., *Optical coherence tomography.* Science, 1991. **254**(5035): p. 1178-1181.
2. Youngquist, R.C., S. Carr, and D.E.N. Davies, *Optical coherence-domain reflectometry - a new optical evaluation technique.* Optics Letters, 1987. **12**(3): p. 158-160.
3. Ralston, T.S., et al., *Interferometric synthetic aperture microscopy.* Nature Physics, 2007. **3**(2): p. 129-134.
4. Izatt, J.A., et al., *Optical coherence microscopy in scattering media.* Optics Letters, 1994. **19**(8): p. 590-592.
5. Fercher, A.F., et al., *Measurement of intraocular distances by backscattering spectral interferometry.* Optics Communications, 1995. **117**(1-2): p. 43-48.
6. Häusler, G. and M.W. Lindner, *"Coherence radar" and "spectral radar"—new tools for dermatological diagnosis* Journal of Biomedical Optics, 1998. **3**(21): p. 21-31.
7. Leitgeb, R., C.K. Hitzenberger, and A.F. Fercher, *Performance of fourier domain vs. time domain optical coherence tomography.* Optics Express, 2003. **11**(8): p. 889-894.
8. Wojtkowski, M., et al., *Ultrahigh-resolution, high-speed, Fourier domain optical coherence tomography and methods for dispersion compensation.* Optics Express, 2004. **12**(11): p. 2404-2422.
9. Fercher, A.F., et al., *Optical coherence tomography - principles and applications.* Reports on Progress in Physics, 2003. **66**(2): p. 239-303.
10. de Boer, J.F., et al., *Improved signal-to-noise ratio in spectral-domain compared with time-domain optical coherence tomography.* Optics Letters, 2003. **28**(21): p. 2067-2069.
11. Choma, M.A., et al., *Sensitivity advantage of swept source and Fourier domain optical coherence tomography.* Optics Express, 2003. **11**(18): p. 2183-2189.
12. Boulnois, *Photophysical processes in recent medical laser developments: A Review.* Lasers in Medical Science, 1985. **1**: p. 47-66.
13. Schuman, J.S., C.A. Puliafito, and J.G. Fujimoto, *Optical coherence tomography of ocular diseases.* 2004: SLACK Inc., Thorofare, NJ.
14. Bouma, B.E., et al., *Evaluation of intracoronary stenting by intravascular optical coherence tomography.* Heart, 2003. **89**(3): p. 317-320.
15. Armstrong, J.J., et al., *Quantitative upper airway imaging with anatomic optical coherence tomography.* American Journal of Respiratory and Critical Care Medicine, 2006. **173**(2): p. 226-233.

16.   Boppart, S.A., et al., *Optical coherence tomography: feasibility for basic research and image-guided surgery of breast cancer.* Breast Cancer Research and Treatment, 2004. **84**(2): p. 85-97.

17.   Pitris, C., et al., *Feasibility of optical coherence tomography for high-resolution imaging of human gastrointestinal tract malignancies.* Journal of Gastroenterology, 2000. **35**(2): p. 87-92.

18.   Zagaynova, E., et al., *A multicenter study of optical coherence tomography for diagnosis and guided surgery of bladder cancer.* Journal of Clinical Oncology, 2004. **22**(14): p. 391S-391S.

19.   Gambichler, T., et al., *Characterization of benign and malignant melanocytic skin lesions using optical coherence tomography in vivo.* Journal of the American Academy of Dermatology, 2007. **57**(4): p. 629-637.

20.   Kawakami-Wong, H., et al., *In vivo optical coherence tomography-based scoring of oral mucositis in human subjects: a pilot study.* Journal of Biomedical Optics, 2007. **12**(5): p. 051702.

21.   Escobar, P.F., et al., *Optical coherence tomography as a diagnostic aid to visual inspection and colposcopy for preinvasive and invasive cancer of the uterine cervix.* International Journal of Gynecological Cancer, 2006. **16**(5): p. 1815-1822.

22.   Whiteman, S.C., et al., *Optical coherence tomography: real-time imaging of bronchial airways microstructure and detection of inflammatory/neoplastic morphologic changes.* Clinical Cancer Research, 2006. **12**(3): p. 813-818.

23.   Bohringer, H.J., et al., *Time-domain and spectral-domain optical coherence tomography in the analysis of brain tumor tissue.* Lasers in Surgery and Medicine, 2006. **38**(6): p. 588-597.

24.   Saleh, B.E.A. and M.C. Teich, *Fundamentals of photonics.* Wiley series in pure and applied optics. 1991, New York: Wiley.

25.   Marks, D.L., et al., *Autofocus algorithm for dispersion correction in optical coherence tomography.* Applied Optics, 2003. **42**(16): p. 3038-3046.

26.   Marks, D.L., et al., *Digital algorithm for dispersion correction in optical coherence tomography for homogeneous and stratified media.* Applied Optics, 2003. **42**(2): p. 204-217.

27.   Potton, R.J., *Reciprocity in optics.* Reports on Progress in Physics, 2004. **67**(5): p. 717-754.

28.   Weyl, *Expansion of electro magnetic waves on an even conductor.* Annalen der Physik, 1919. **60**: p. 481–500.

29.   Mandel, L. and E. Wolf, *Optical coherence and quantum optics.* 1996: Cambridge University Press.

30.   Gazdag, J. and P. Sguazzero, *Migration of seismic data.* Proceedings of the IEEE, 1984. **72**(10): p. 1302-1315.

31.   Stolt, R.H., *Migration by Fourier-transform.* Geophysics, 1978. **43**(1): p. 23-48.

32.   Davis, B.J., et al., *Interferometric synthetic aperture microscopy: computed imaging for scanned coherent microscopy.* Sensors, 2008. **8**(6): p. 3903-3931.

33.   Cormack, A.M., *Representation of a function by its line integrals, with some radiological applications.* Journal Applied Physics, 1963. **34**: p. 2722–2727.

34.   Hounsfield, G.N., *Computerized transverse axial scanning (tomography) .1. Description of system.* British Journal of Radiology, 1973. **46**(552): p. 1016-1022.

35.   Devaney, A.J., *Reconstructive tomography with diffracting wavefields.* Inverse Problems, 1986. **2**: p. 161-183.

36.   Pan, S.X. and A.C. Kak, *A Computational study of reconstruction algorithms for diffraction tomography - interpolation versus filtered backpropagation.* IEEE Transactions on Acoustics Speech and Signal Processing, 1983. **31**(5): p. 1262-1275.

37.   Wolf, E., *Three-dimensional structure determination of semi-transparent objects from holographic data.* 1969. **1**: p. 153-156.

38.   Lauterbur, P.C., *Image formation by induced local interactions - examples employing nuclear magnetic-resonance.* Nature, 1973. **242**(5394): p. 190-191.

39.   Born, M. and E. Wolf, *Principles of optics : electromagnetic theory of propagation, interference and diffraction of light.* 7th ed. 1999, New York: Cambridge University Press.

40.   Richards, B. and E. Wolf, *Electromagnetic diffraction in optical systems. II. Structure of the image field in an aplanatic system.* Proceedings Royal Society of London, Series A, 1959. **253**: p. 358-379.

41.   Davis, B.J., et al., *Nonparaxial vector-field modeling of optical coherence tomography and interferometric synthetic aperture microscopy.* Journal of the Optical Society of America A, 2007. **24**(9): p. 2527-2542.

42.   Marks, D.L., et al., *Inverse scattering for frequency-scanned full-field optical coherence tomography.* Journal of the Optical Society of America A, 2007. **24**(4): p. 1034-1041.

43.   Marks, D.L., et al., *Partially coherent illumination in full-field interferometric synthetic aperture microscopy.* Journal of the Optical Society of America A, (in press).

44.   Marks, D.L., et al., *Inverse scattering for rotationally scanned optical coherence tomography.* Journal of the Optical Society of America A, 2006. **23**(10): p. 2433-2439.

45.   Zhao, Y.H., et al., *Phase-resolved optical coherence tomography and optical Doppler tomography for imaging blood flow in human skin with fast scanning speed and high velocity sensitivity.* Optics Letters, 2000. **25**(2): p. 114-116.

46.   Choma, M.A., et al., *Spectral-domain phase microscopy.* Optics Letters, 2005. **30**(10): p. 1162-1164.

47.   Joo, C., et al., *Spectral-domain optical coherence phase microscopy for quantitative phase-contrast imaging.* Optics Letters, 2005. **30**(16): p. 2131-2133.

48.   Yang, C., et al., *Phase-referenced interferometer with subwavelength and subhertz sensitivity applied to the study of cell membrane dynamics.* Optics Letters, 2001. **26**(16): p. 1271-1273.

49.   Rylander, C.G., et al., *Quantitative phase-contrast imaging of cells with phase-sensitive optical coherence microscopy.* Optics Letters, 2004. **29**(13): p. 1509-1511.

50.   de Boer, J.F., et al., *Two-dimensional birefringence imaging in biological tissue by polarization-sensitive optical coherence tomography.* Optics Letters, 1997. **22**(12): p. 934-936.

51.   Tomlins, P.H. and R.K. Wang, *Digital phase stabilization to improve detection sensitivity for optical coherence tomography.* Measurement Science & Technology, 2007. **18**(11): p. 3365-3372.

52.   Adler, D.C., et al., *Optical coherence tomography contrast enhancement using spectroscopic analysis with spectral autocorrelation.* Optics Express, 2004. **12**(22): p. 5487-5501.

53.   Xu, C.Y., et al., *Spectroscopic spectral-domain optical coherence microscopy.* Optics Letters, 2006. **31**(8): p. 1079-1081.

54.   Adler, D.C., R. Huber, and J.G. Fujimoto, *Phase-sensitive optical coherence tomography at up to 370,000 lines per second using buffered Fourier domain mode-locked lasers.* Optics Letters, 2007. **32**(6): p. 626-628.

55.   Vakhtin, A.B., et al., *Common-path interferometer for frequency-domain optical coherence tomography.* Applied Optics, 2003. **42**(34): p. 6953-6958.

56.   Jackson, D.A., et al., *Elimination of drift in a single-mode optical fiber interferometer using a piezoelectrically stretched coiled fiber.* Applied Optics, 1980. **19**(17): p. 2926-2929.

57.   Lin, D., et al., *High stability multiplexed fiber interferometer and its application on absolute displacement measurement and on-line surface metrology.* Optics Express, 2004. **12**(23): p. 5729-5734.

58.   Ralston, T.S., et al., *Phase stability technique for inverse scattering in optical coherence tomography*, in *IEEE International Symposium on Biomedical Imaging.* April 6-9, 2006: Arlington, VA.

59.   Leitgeb, R.A., et al., *Real-time measurement of in vitro flow by Fourier-domain color Doppler optical coherence tomography.* Optics Letters, 2004. **29**(2): p. 171-173.

60.   Lerner, S.P., et al., *Optical coherence tomography as an adjunct to white light cystoscopy for intravesical real-time imaging and staging of bladder cancer.* Urology, 2008. **72**(1): p. 133-137.

61.   Park, B.H., et al., *Real-time multi-functional optical coherence tomography.* Optics Express, 2003. **11**(7): p. 782-793.

62.   Wojtkowski, M., et al., *Real-time in vivo imaging by high-speed spectral optical coherence tomography.* Optics Letters, 2003. **28**(19): p. 1745-1747.

63.   Yun, S.H., et al., *High-speed spectral-domain optical coherence tomography at 1.3 µm wavelength.* Optics Express, 2003. **11**(26): p. 3598-3604.

64.   Ralston, T.S., et al., *Real-time interferometric synthetic aperture microscopy.* Optics Express, 2008. **16**(4): p. 2555-2569.

65.   Yaroslavsky, L., *Boundary effect free and adaptive discrete signal sinc-interpolation algorithms for signal and image resampling.* Applied Optics, 2003. **42**(20): p. 4166-4175.

66.   Pan, Y.T., R. Birngruber, and R. Engelhardt, *Contrast limits of coherence-gated imaging in scattering media.* Applied Optics, 1997. **36**(13): p. 2979-2983.

67.   Yadlowsky, M.J., J.M. Schmitt, and R.F. Bonner, *Multiple-scattering in optical coherence microscopy.* Applied Optics, 1995. **34**(25): p. 5699-5707.

68.   Chen, Y., et al., *Ultrahigh resolution optical coherence tomography of Barrett's esophagus: preliminary descriptive clinical study correlating images with histology.* Endoscopy, 2007. **39**(7): p. 599-605.

69.   Wang, Z.G., et al., *In vivo bladder imaging with microelectromechanical systems-based endoscopic spectral domain optical coherence tomography*. Journal of Biomedical Optics, 2007. **12**(3): p. 034009.

70.   Hsiung, P.L., et al., *Ultrahigh-resolution and 3-dimensional optical coherence tomography ex vivo imaging of the large and small intestines*. Gastrointestinal Endoscopy, 2005. **62**(4): p. 561-574.

71.   Fujimoto, J.G., *Optical coherence tomography for ultrahigh resolution in vivo imaging*. Nature Biotechnology, 2003. **21**(11): p. 1361-1367.

72.   Fujimoto, J.G., et al., *Optical coherence tomography: an emerging technology for biomedical imaging and optical biopsy*. Neoplasia, 2000. **2**(1-2): p. 9-25.

73.   Drexler, W., *Ultrahigh-resolution optical coherence tomography*. Journal of Biomedical Optics, 2004. **9**(1): p. 47-74.

74.   Cellini, C., et al., *Factors associated with residual breast cancer after re-excision for close or positive margins*. Annals of Surgical Oncology, 2004. **11**(10): p. 915-920.

75.   Nguyen, F.T., et al. *Portable real-time optical coherence tomography system for intraoperative imaging and staging of breast cancer*. 2007. San Jose, CA, United States: SPIE -International Society for Optical Engineering, Bellingham WA, WA 98227-0010, United States.

76.   Luo, W., et al., *Optical biopsy of lymph node morphology using optical coherence tomography*. Technology in Cancer Research & Treatment, 2005. **4**(5): p. 539-547.

77.   Povazay, B., et al., *Submicrometer axial resolution optical coherence tomography*. Optics Letters, 2002. **27**(20): p. 1800-1802.

78.   Huang, Q., et al., *Noninvasive visualization of tumors in rodent dorsal skin window chambers - a novel model for evaluating anti-cancer therapies*. Nature Biotechnology, 1999. **17**(10): p. 1033-1035.